In vivo imaging of human vasculature in the chorioretinal complex using phase-variance contrast method with phase-stabilized 1-µm swept-source optical coherence tomography

Raju Poddar
Dae Yu Kim
John S. Werner
Robert J. Zawadzki

In vivo imaging of human vasculature in the chorioretinal complex using phase-variance contrast method with phase-stabilized 1-μm swept-source optical coherence tomography

Raju Poddar,[a,b] Dae Yu Kim,[a,c] John S. Werner,[a] and Robert J. Zawadzki[a,*]
[a]University of California Davis, Department of Ophthalmology and Vision Science, Vision Science and Advanced Retinal Imaging Laboratory, Sacramento, California 95817, United States
[b]Birla Institute of Technology, Department of Biotechnology, Mesra, Ranchi, Jharkhand 835215, India
[c]Dankook University, Beckman Laser Institute Korea, Cheonan, Chungnam 330-715, Republic of Korea

Abstract. We present a noninvasive phase-variance (pv)–based motion contrast method for depth-resolved imaging of the human chorioretinal complex microcirculation with a newly developed phase-stabilized high speed (100-kHz A-scans/s) 1-μm swept-source optical coherence tomography (SSOCT) system. Compared to our previous spectral-domain (spectrometer based) pv-spectral domain OCT (SDOCT) system, this system has the advantages of higher sensitivity, reduced fringe wash-out for high blood flow speeds and deeper penetration in choroid. High phase stability SSOCT imaging was achieved by using a computationally efficient phase stabilization approach. This process does not require additional calibration hardware and complex numerical procedures. Our phase stabilization method is simple and can be employed in a variety of SSOCT systems. Examples of vasculature in the chorioretinal complex imaged by pv-SSOCT from normal as well as diseased eyes are presented and compared to retinal images of the same subjects acquired with fluorescein angiography and indocyanine green angiography. Observations of morphology of vascular perfusion in chorioretinal complex visualized by our method are listed. © *The Authors. Published by SPIE under a Creative Commons Attribution 3.0 Unported License. Distribution or reproduction of this work in whole or in part requires full attribution of the original publication, including its DOI.* [DOI: 10.1117/1.JBO.19.12.126010]

Keywords: optical coherence tomography; retinal blood flow; ophthalmic optics and devices; ophthalmology; medical and biological imaging; medical optics instrumentation.

Paper 140239PR received Apr. 15, 2014; revised manuscript received Jul. 17, 2014; accepted for publication Oct. 8, 2014; published online Dec. 17, 2014.

1 Introduction

Numerous ocular diseases including myopia, central serous chorioretinopathy, and age-related macular degeneration (AMD) are found to be linked to changes in the choroid.[1,2] Most of the current clinical optical coherence tomography (OCT) technology, mainly spectral domain OCT, utilizes the 800 to 950-nm spectral window. This technology permits efficient measurements of retinal structures, including vessels and capillaries, but provides limited ability to examine the layered vasculature beds of the choroid. This is mainly because the 800 to 950-nm band light is strongly scattered and absorbed by the melanin in both the retinal pigment epithelium (RPE) and the choroid; thus, its penetration into the deep choroid is limited. It has been demonstrated that in order to obtain higher penetration into the choroid, one can use the 1 to 1.1-μm spectral band for OCT.[3] Despite increased absorption by water for longer wavelengths, the low absorption by melanin at a wavelength of around 1.05 μm and the presence of the water absorption minimum in the same range enables higher penetration into the choroid. Although several groups have demonstrated retinal SD-OCT at 1 μm, performance for angiographic imaging has been limited by strong fringe washout due to the high blood flow in the choroid, a

short depth range and a rapid sensitivity drop off.[4] Thanks to advances in laser swept sources, swept-source (SS) OCT is now an attractive alternative for imaging in the 1-μm range over SD-OCT. Its main advantages include robustness to sample motion,[5,6] a long measurement range in depth due to short instantaneous line-width,[7] linear sampling in wavenumber (k-clock—trigger), compactness, increased detection efficiency (balance detection scheme), and high imaging speed.[8] With current commercially available swept sources, imaging the retina at 100 kHz compared with ~25 to 60 kHz in most commercial SD-OCT systems can be easily achieved in clinical swept-source optical coherence tomography (SSOCT) instruments without a reduction in sensitivity: for example DRIOCT-1, TOPCON SSOCT.[9]

Importantly, progress in phase stabilization schemes[10–13] and lack of fringe washout artifacts permit reliable mapping of fast flows. There are several methods for increasing the contrast of vessels using the Doppler effect present in OCT data sets, such as Doppler standard deviation imaging,[14] optical coherence angiography (OCA),[15,16] phase-variance (pv) OCT,[17–19] and joint spectral and time domain OCT.[20] Here, pvOCT[19] methods were implemented in our laboratory to extract flow contrast from SSOCT images, resulting in the visualization of volumetric microvasculature perfusion independent of vessel orientation.

Standard SSOCT systems often suffer from jitter in synchronization between the wavelength sweep and data acquisition

*Address all correspondence to: Robert J. Zawadzki, E-mail: rjzawadzki@ucdavis.edu

timing; this jitter causes small random spectral shifts among interference spectra and results in phase instability between A-scans. This phase instability is a critical problem for phase-sensitive OCT modalities including pv OCT. The problem can be partially resolved by utilizing a stationary mirror or a glass plate in the sample arm.[10] It also requires additional hardware in the sample arm, thus it makes the system more complicated and limits the depth measurement range. Another approach to stabilize the phase is by using a separate Mach–Zehnder interferometer from an OCT main interferometer[11] or numerical phase stabilization OCA.[12] Recently, one phase stabilization method was reported using a fiber Bragg grating (FBG) at one of the detection arms.[21] This system demonstrated good phase stability without sacrificing depth imaging range, but it still required additional hardware and was computationally complex. The same group later demonstrated the capability of an SSOCT prototype at 1060-nm wavelengths with a 400-kHz A-scan for *in vivo* imaging of choriocapillaris and choroidal microvasculature in normal human subjects using a speckle decorrelation method.[22] They presented results for choriocapillaris imaging over a 1.5×1.5-mm^2 area on the retina. However, their algorithm for calculating speckle decorrelation is limited by bulk motion removal in the axial direction. We have recently described[23] a simple method for phase stabilization using an A-line trigger from a fixed wavenumber FBG and numerical phase stabilization, without any major additional calibration hardware changes. Here, we describe modifications of this system allowing mapping of vascular beds in different layers of the chorioretinal complex of normal and diseased human eyes *in vivo*.

2 Materials and Methods

2.1 Phase-Variance SSOCT System

A schematic diagram of our 1-μm SSOCT system used for anterior segment imaging has been previously reported.[23] Here, we briefly describe changes to our SSOCT system (Fig. 1) that allowed posterior segment imaging. The light source was an external cavity tunable laser, SS laser (Axsun Technologies), with a central wavelength of 1060 nm, sweep bandwidth of 110 nm, repetition rate of 100 kHz, 46% duty cycle and average output power of ~23 mW. A spectrally balanced interferometer configuration was used with three 50/50 fiber couplers (AC Photonics), and a balanced Mach–Zehnder fiber interferometer.[8] The sample port was attached to a probe unit, which comprises a fiber collimator lens (12.38 mm, focal length, TC12APC-1064, Thorlabs, Inc.), two single-axis (X-Y) scanners (Cambridge Technology), and two achromatic doublets of focal length 50 and 30 mm. The reference port of the fiber coupler was attached to a reference arm unit comprising a collimator lens, an achromatic doublet lens, dispersion compensating block, and a static silver-coated mirror.

2.2 Image Acquisition and Data Processing for pv-SSOCT

The galvanometric scanners that steer the probe beam were controlled by a data acquisition (DAQ) card (PCI-6363, National Instruments, Texas). The probing beam power at the sample was set at 1.85 mW, which is lower than the ANSI limit for safe light exposure (ANSI Z136.1 standard). The reflected beams from both arms of the interferometer were combined at the couplers and detected by a balanced photodetector with a bandwidth of DC to 350 MHz (PDB130C, Thorlabs Inc.) followed by an RF amplifier and high pass filter (Minicircuits ZFL-1000+). The OCT interference signal was digitized by a DAQ board at 12-bit digital resolution at a sampling rate defined by the external trigger provided by the Axsun SS k-clock (ATS9350, AlazarTech, QC, Canada).

Here, a simple method[23] for phase stabilization was implemented. It also reduces A-line trigger fluctuations from the laser source. A fixed wavelength reference signal generated by an FBG (OE Land, Quebec, Canada, $\lambda_0 = 988.9$ nm, reflectivity $= 99.91\%$, $\Delta\lambda = 0.4$ nm) inserted in a transmission mode between the source and the OCT interferometer (Fig. 1) was used to align the start time of each A-line in postprocessing.
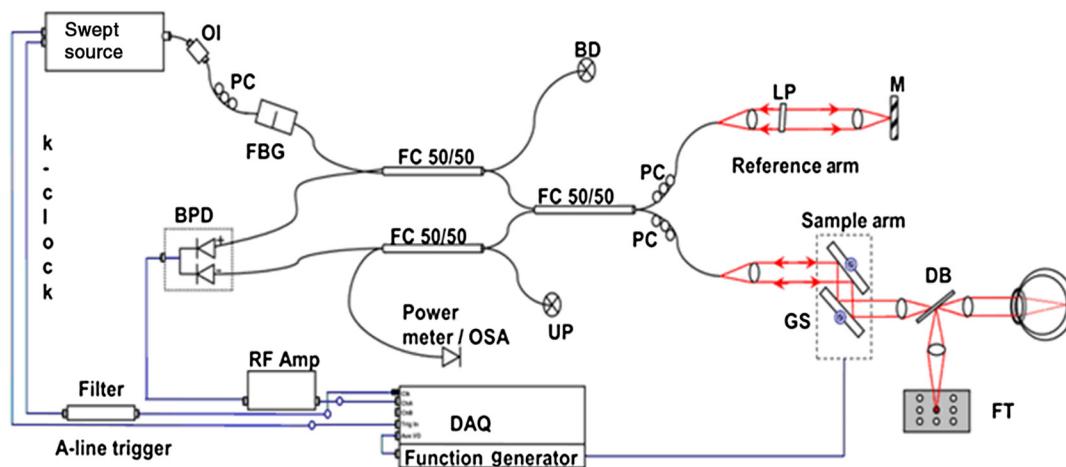

Fig. 1 Schematic diagram of phase-variance-swept source optical coherence tomography (pv-SSOCT) system. Swept source laser 1060-nm Axsun ECTL. FBG: fiber Bragg grating, FC: fiber coupler, GS: galvanometric scanning mirrors, M: mirror, BPD: balanced photodiode receiver (DC to 350 MHz, PDB130C, Thorlabs), PC: polarization controller, LP: linear polarizer, RF Amp: radio frequency amplifier (Minicircuits ZFL-1000+), DB: dichroic beamsplitter, FT: fixation target, BD: beam dump, UP: unused port, OSA: optical spectrum analyzer, DAQ: digitizer (ATS9350, AlazarTech, 12-bit resolution and sampling rate of 500 MS/s), function generator (NI PCI-6363 DAQ, National Instruments, Texas).

Due to slight mismatch in the intensity of dual balance detection channels of our intereferometer, the reference signal generated by the FBG can be easily detected. Note, however, that in a perfectly balanced OCT detection system, this method would not work as the FBG reference signal could not be detected. The necessary shifts[21,23] in the acquired SSOCT signal can be calculated based on the first falling slope of the signal around the FBG signal. This phase stabilization method was adopted before pv calculation. The accuracy of phase-stabilization is discussed in Sec. 2.3. This results in measurement of phase-shifts at a noise level down to the theoretical limit (see Sec. 2.3.1), thereby allowing complete removal of fixed-pattern noise and artifact-free pv contrast images.

Synchronization between data acquisition and the scanners is achieved in the build sweep trigger signal of the laser source, which is utilized for triggering the data acquisition of the DAQ for a single sweep and additionally as an update clock for the waveform generation for the galvo scanners. The subject's gaze was reduced by using a custom-built fixation target reflected through a dichroic beamsplitter (FF775-Di01, Semrock). The fixation target is a mini LCD screen (MIMO) controlled by computer to allow movement for precalibrated fixation light positions. Data acquisition with LabVIEW software (National Instruments) required 1 to 2 s depending on the scanning pattern settings. The raw data are saved in the PC workstation (HP xw8600, 3.2-GHz dual processors). Data sampling was performed using an optically generated clock signal with equi-spacing in wavenumber, namely, a k-clock from the laser source. Due to this k-linear sampling, no rescaling process is required before Fourier transform of the spectral data. To validate the performance of our system on different eyes, the pv-SSOCT data sets were obtained in the Vision Science and Advanced Retinal Imaging laboratory (VSRI) at the University of California Davis Medical Center on two normal subjects with normal ocular media (Subject 1: 62 year-old male and Subject 2: 27 year-old male) and four AMD patients (P1: 62 year-old male; P2: 57 year-old female; P3: 55 year-old male; P4: 73 year-old male). Written informed consent was obtained prior to imaging using a protocol approved by the UC Davis Institutional Review Board. Subject's head position was fixed during acquisition using a custom bite-bar and forehead rest. 1% Tropicomide was used for cycloplegia and pupil dilation. A BM-scanning mode [acquisition of multiple B-scans at the same position, similar to M-mode (motion mode) in ultrasound] was used to acquire the phase-change measurements required to calculate the pv contrast. For the 1.5×1.5-mm^2 scanning pattern, 4.2-μm spacing between both consecutive A-scans and BM-scans was used. Due to the spatial oversampling between consecutive BM-scans, phase changes from within two adjacent BM-scans were used for the variance calculations. Three B-scans were acquired within each BM-scan, producing two phase change measurements for each BM-scan. The A-line exposure time was 4.2 μs and the spectral data were saved in a binary file format for postprocessing in LabVIEW software. All images shown in this manuscript were acquired *in vivo* at a rate of 100,000 axial scans (A-scan) per second.

Each OCT data set (A-scan, already sampled linearly in k-space) was first aligned "in time" based on the reference FBG signal position. After finishing this step, fixed-pattern noise was removed by subtracting the averaged B-scan spectrum from each individual A-line spectrum. The resultant spectra were windowed to minimize side-lobes of the coherence function by apodization with a flat top Gaussian window. Residual mismatch between sample and reference arm dispersions was numerically compensated by automatic dispersion compensation based on an entropy minimization method.[16] Finally, a complex SSOCT image with intensity and phase information was obtained after Fourier transformation of the processed and zero padded (to 4096 points) data.

OCT signal sensitivity fall-off profiles for our 1060-nm system were measured using standard procedures[6,7] and reported in our previously published report.[23] Each B-scan consisted of 440 A-scans with 375 A-scans acquired over a 1.5-mm lateral scanning range on the retina and 65 "fly-back" A-scans. The dynamic range of the intensity image was 35 dB and the phase values varied from $-\pi$ to $+\pi$. The basic concept of the pv-based motion contrast method has been described in our previous papers.[19] The acquired and preprocessed OCT data sets were postprocessed by software developed at the Biological Imaging Center at the California Institute of Technology to extract pv signals. The cross-correlation function between consecutive intensity images aligns each B-scan from a BM-scan in an axial direction. Phase unwrapping on phase difference values, bulk motion removal, and histogram-based thresholding were implemented to remove phase shifts caused by eye and head movements. To visualize depth-resolved vasculature networks projections in the chorioretinal complex, the three-dimensional (3-D) pv data sets were manually segmented into three layers as per prior literature. The *en face* projection view of the segmented data produced two-dimensional (2-D) vascular perfusion maps, which are similar to the ones obtained with fundus FA. For comparison, FA and indocyanine green angiography (ICGA) images were acquired with the Topcon (TRC-50IX) fundus camera and Heidelberg Spectralis™ HRA + OCT. The images consisted of $1536 \text{(H)} \times 1536 \text{(V)}$ pixels over a 30-deg field-of-view (FOV) on the retina. All of these clinical images were taken with fully dilated pupils. Pseudocolor [red-green-blue (RGB)] depth coding of the processed pv-OCT volumetric data sets was used to better visualize 3-D vessel networks and its projection view created 2-D color vasculature maps linearly color coded by axial depth location of the vessels.

2.3 Phase Stability Analysis

The accuracy of pv measurements and the removal of fixed-pattern noise both depend on the phase stability of the SSOCT system. Phase stability can be measured by analyzing the phase difference between successive A-lines as measured at the same location on a stationary mirror.[11–13] The phase noise, σ_Δ, defined as the standard deviation of phase difference values, follows a Gaussian probability distribution. The phase stability performance (as a function of path-length difference between sample and reference arms) was measured by phase difference values from the stationary mirror. At each depth (mirror position), 4000 subsequent A-lines were taken which were split into four data sets of 1000 A-lines. The phase-noise $\sigma_{\Delta\varnothing}$ of each data set, plotted in Fig. 2, was calculated by taking the standard deviation of the phase difference values as well as the mean and standard deviation over $\sigma_{\Delta\varnothing}$ from all four data sets. The prestabilized data were calculated without FBG reference signal correction between the A-lines. The measured values for $\sigma_{\Delta\varnothing}$ are plotted against depth as red symbols for the case-with and as blue dots for the case-without phase stabilization. The measured
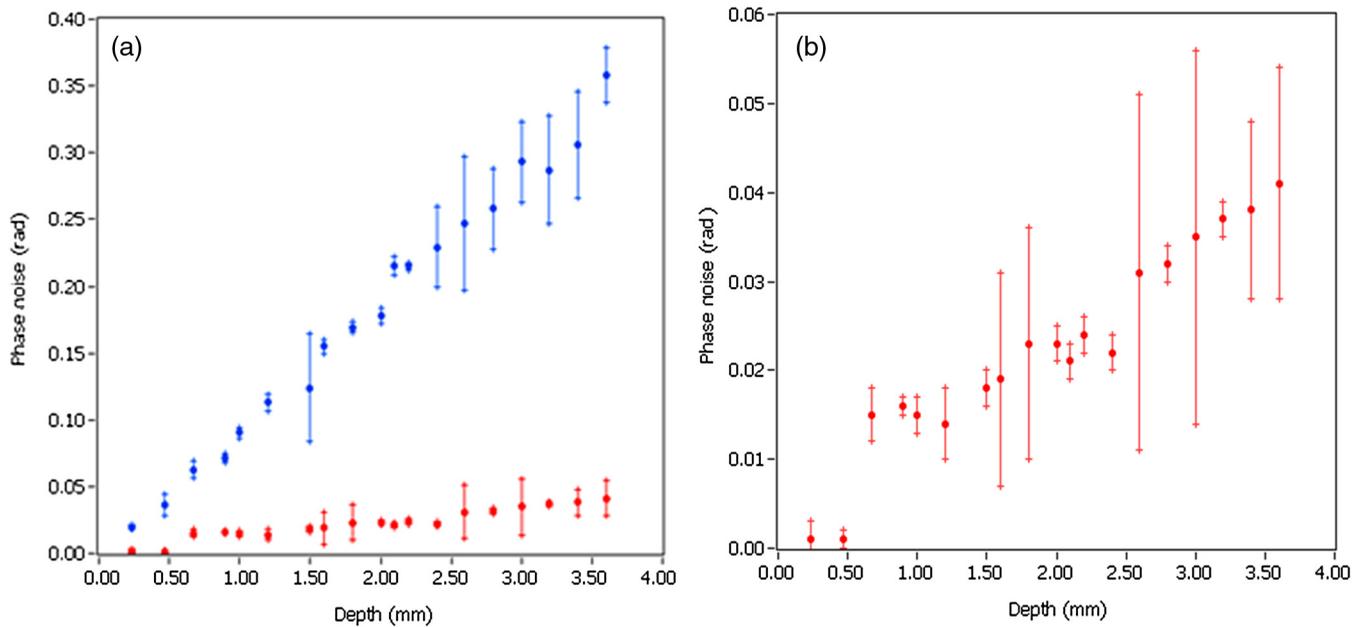
Fig. 2 (a) The phase noise in radians with (red) and without (blue) phase stabilization is plotted against depth of the mirror placed in the sample arm. Error bars denote the standard deviation of the measurements. The phase noise is significantly lower when phase stabilization is used, especially at greater depths. (b) The zoom-in view of the phase noise measured with phase stabilization.

standard deviations of these measurements are displayed as vertical error bars. We can conclude from the figure that the phase noise is considerably lower (up to about 40 times at greater depths) when phase stabilization is used. In Fig. 2(b), a zoomed part of Fig. 2(a) (red), phase noise measured with phase stabilization is shown.

A mean phase noise value of 30 mrad was measured at a depth of 1.5 mm. An SNR value of 50 dB was used to calculate the phase-noise in Fig. 2. This is comparable to previously published results for SSOCT systems phase noise (e.g., Hendargo et al.[13] reported 18 mrad for 53-dB SNR, and Baumann et al.[10] reported 97 mrad at 100 kHz and 47 mrad at 200 kHz for a 35-dB SNR).

2.4 Imaging Performance

Here, we present images demonstrating the effects of fixed pattern noise removal on intensity-based OCT and pv-OCT images.

2.4.1 Fixed-pattern noise removal

The effect of fixed-pattern noise removal is shown in an intensity image of the macula of a healthy volunteer (Fig. 3). The image has a width of 5 mm consisting of 1500 A-lines and a displayed depth of 2.8 mm.

The image quality is degraded at several depths by fixed-pattern noise lines [yellow arrow Fig. 3(a)] when no phase stabilization correction is used. The phase-stabilization method allowed DC removal to suppress these artifact lines (fixed-pattern noise) very effectively [Fig. 3(b)].[10–12] With a mirror as an object in the sample arm, the fixed-pattern noise suppression was measured at different depths and showed a reduction of 40 dB at the zero-delay point (data not shown).

2.4.2 Fixed-pattern phase-noise artifact removal in flow mapping

The need to apply the phase-stabilization method before pv-OCT processing is shown in Fig. 4 on B-scans acquired at 6-deg temporal retina. The intensity images are shown in Figs. 4(a) and 4(d). Each intensity B-scan image covers a lateral area of 1.5 mm consisting of 375 A-lines, a displayed depth of 1.5 mm, and a dynamic range of 35.0 dB. The corresponding pv images [Figs. 4(b) and 4(e)] have the same dimensions. A 2-D median filter (3 × 10 pixels) was used for noise reduction. In Fig. 4(b), the pv image is shown when the phase-stabilization
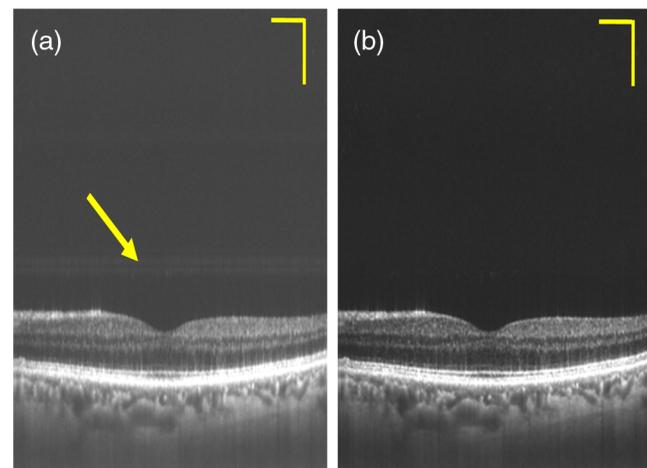

Fig. 3 Fixed-pattern noise removal on an SSOCT intensity image of the macula of a healthy volunteer (Subject 1). (a) The image without fixed-pattern noise removal when the phase stabilization method is not used. Artifact (coherent noise) lines are clearly visible above the retina. (b) Fixed-pattern noise removal on a phase-stabilized image. Scale bar: 500 μm.
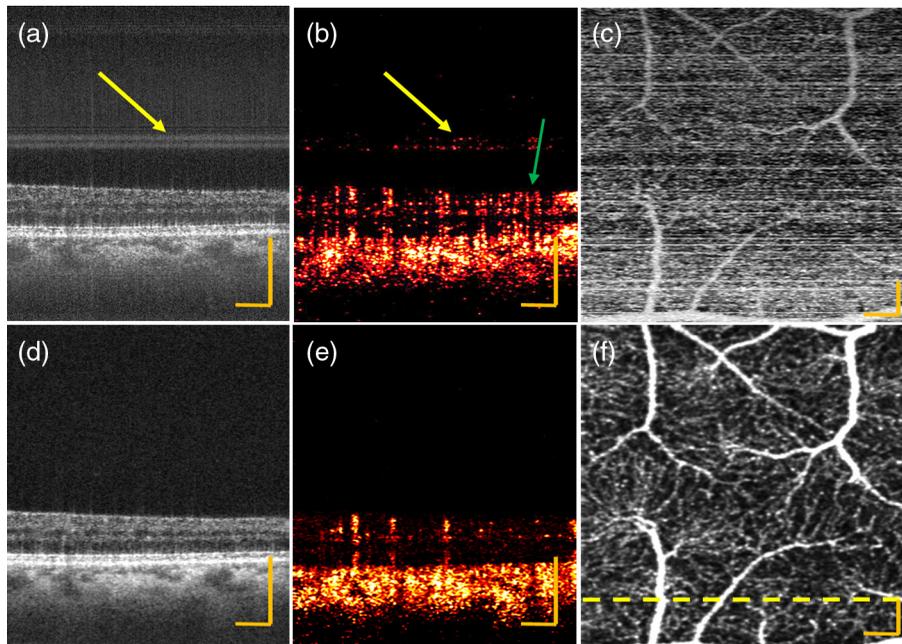
Fig. 4 Top and bottom panels show images before and after phase stabilization, respectively. Average intensity image of three B-scans (a and d). pv processed image using phase data from the same three B-scans (b and e), *en face* projection of retinal vasculature (c and f); yellow dashed line in panel (f) shows the location of B-scan. Vertical phase artifact lines (yellow arrows) and horizontal lines (green arrow) can be seen throughout the images processed without phase stabilization (a and b). Scale bar: 300 μm.

method was not used, which resulted in horizontal (yellow arrow) as well as vertical (green arrow) phase-artifacts throughout the B-scan, obscuring a clear view of the detected blood flow. These artifacts are, however, absent when the phase-stabilization method was used as shown in Fig. 4(e). The same effect can be observed on *en face* projection images in Figs. 4(c) and 4(f).

3 Results and Discussion

The performance of the phase-stabilized pv-SSOCT for *in vivo* imaging of blood flow was demonstrated by imaging various positions of the posterior segment of a healthy volunteer. The pv image provides complementary information about the vasculature that is hard to observe in the intensity image. The pv B-scan images were manually segmented and integrated over depth to create an intensity *en face* image of the

chorioretinal vasculature. The visualization of a different part of the chorioretinal complex vasculature by phase-stabilized pv-SSOCT has the potential for early detection of pathology.

3.1 Three-Dimensional Imaging of the Chorioretinal Vascular Network

To extract chorioretinal vasculature from BM-scans, pvOCT data were acquired over a 1.5×1.5-mm^2 area of the human retina with an A-scan sampling spacing of 4 μm (between consecutive A-scans) for clear visualization of microcirculation. The scanning beam was focused on the RPE to improve visualization of the outer retinal layers and the blood supply in the choroid and choriocapillaris. An average intensity image composed of three successive B-scans from a single BM-scan is shown in Fig. 5(a). Figure 5(b) shows the image postprocessed
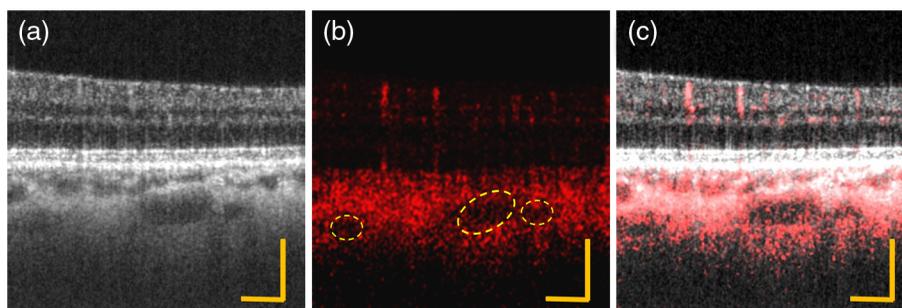

Fig. 5 Images of human retina acquired over 1.5 mm. (a) Average intensity of three B-scans from one BM-scan sequence. (b) pv image coded as red. (c) Composite B-scan image showing flow signal in different layers overlaid over intensity image (gray) (a) and pv image (red) (b). The imaging acquisition time of a single BM-scan containing three B-scans is ~10.5 ms. Yellow ovals are drawn around vessels in Haller's layer. Scale bar: 300 μm.
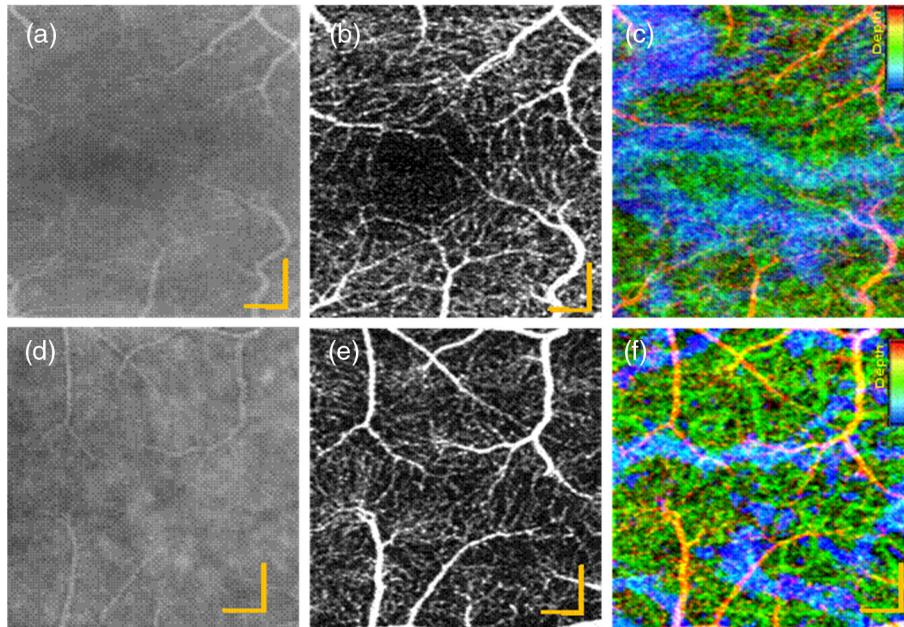
Fig. 6 *In vivo* human retinal vasculature images (1.5×1.5 mm^2) from a normal subject at foveal (upper panel) and 6-deg temporal retina (lower panel). (a and d) Fluorescein angiography (FA) images. (b and e) Projection view of retinal contributions to pvOCT. The numbers of A-scans and B-scans are 375 and 360, respectively, (c and f). RGB depth color-coded projection view of pvOCT data. Upper right shows depth scale bar with red color denoting a retinal layer, green showing capillaries as choroidal vascular bed, whereas blue represents capillaries in deeper choroidal layers. The imaging acquisition time was 3.6 s. Scale bar: 500 μm. Video 1 shows C-scan fly through the three-dimensional pvOCT data set (MOV 4066KB) [URL: http://dx.doi.org/10.1117/1.JBO.19.12.126010.1]..

with the pv method from these data. The composite image with averaged intensity (gray image) and pv (red image) is shown in Fig. 5(c). There was no significant eye motion during BM-scan acquisition due to the short acquisition times of each B-scan (approximately 3.5 ms). The composite image validates that the pvOCT identifies most perfused vessels as identified on the averaged intensity images where vessels can be classified based on the change in intensity (bright dots located near inner and outer plexiform layers). One can also observe a shadow artifact that generates residual pv values below vessels. We think that this is caused by variation in the optical path-length (phase) of photons passing through blood flowing in these vessels. This effect creates nonzero pv values calculated in retinal layers where no perfusion should be observed, including in the retinal-pigmented epithelium and deep choroidal layers. There is also loss in the pv signal from deeper choroid (larger vessels in Haller's layer) due to very fast blood flow; they appear as dark areas in pv images [yellow circles in Fig. 5(b)]. More pv signal in deeper choroid was observed compared to our previously reported SD-OCT-based pv.[19] This was possible due to the higher OCT sensitivity in SSOCT, and the use of a 1060-nm central wavelength increased penetration depth, thus improving contrast below the RPE. Additional benefits include extended measurement range in depth due to short instantaneous line-width of the source and permitting OCT imaging at distances further away from the zero path-length difference than is
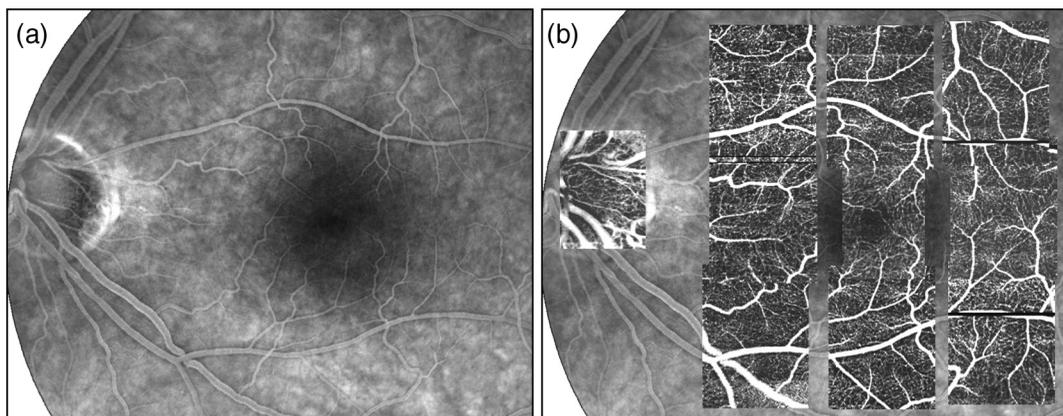

Fig. 7 Large field-of-view (FOV) stitched pvOCT imaging overlaid on a fundus FA. (a) FA. (b) Projection view of retinal contributions to pvOCT imaging with the 10 volumes.
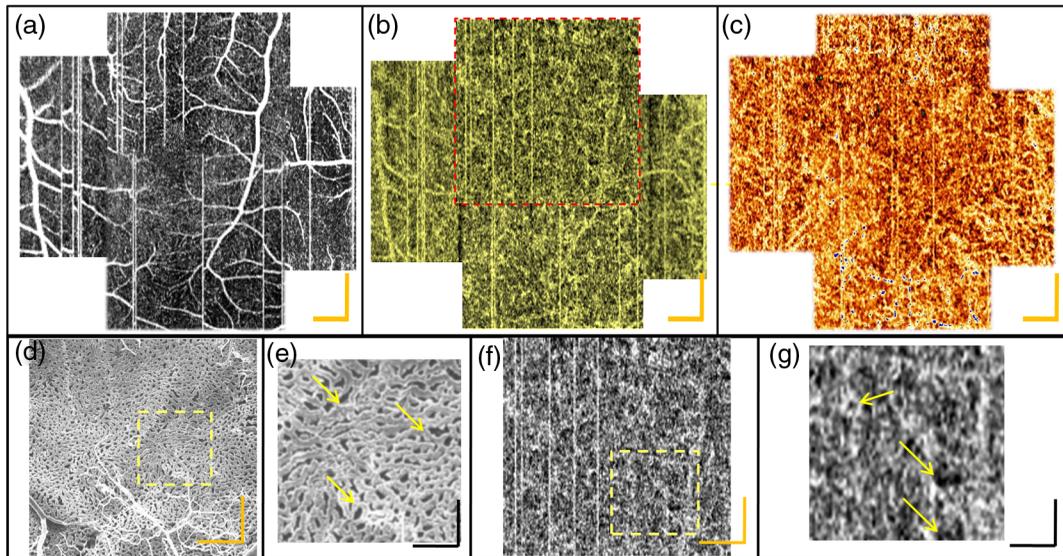
Fig. 8 Mosaic view of pvSSOCT imaging of a normal subject (2) from central foveal region. (a) Projection view of retinal layers (b) Stitched OCT angiograms of the choriocapillaris, and (c) Sattler's layer. Scale bar: 400 μm. (d) *In-vitro* scanning electron microscopy image from a methyl methacrylate cast of an excised eye27 which shows the subfoveal choriocapillaris microstructures in high-resolution for a 1.4 $\times$ 1.4-mm^2 area. (e) A magnified view on a 450 $\times$ 450-μm^2 area of the choriocapillaris angiogram [marked yellow in (d)] to show individual pores in detail (indicated with three yellow arrows). (F) *In vivo* angiogram of the choriocapillaris with pvSSOCT showing a similar mesh-like network of small vessels with small black pores for a 1.5 $\times$ 1.5-mm^2 area (volume section highlighted with red dotted lines in (b). (g) A magnified view from (f) for a 450 $\times$ 450-μm^2 area [marked yellow in (f)] in which yellow arrows indicate pores with a similar size as those observed in (e).The choriocapillaris angiogram of (d) shows similar microstructures as in (f). The yellow scale-bars are 300 μm in length; the black scale-bars are 50 μm in length.

possible with spectrometer-based OCT systems. Thus, even with modest axial head motion of the patient from the forehead rest during automatic acquisition of several volumes, image quality was not impaired by relative changes of the location of the imaged structures with respect to the reference arm position.

3.2 *Pv-SSOCT Vascular Network Imaging of Chorioretinal Complex in Normal Eyes*

Eyes from two normal subjects were imaged with the pv-SSOCT system. The images illustrated in Fig. 6 were acquired over 1.5 $\times$ 1.5 mm^2 at two eccentricities (fovea and 6-deg temporal retina). We compared maximum projection views of

pvOCT in Figs. 6(c) and 6(f) to the fundus FA in Figs. 6(b) and 6(e), respectively, acquired at the same location. Figures 4(b) and 4(e) show dense microcapillary networks around the foveal avascular zone and temporal zone, not distinctly recognizable in the zoomed fundus FA image. The size of the smallest resolvable capillary in this acquisition scheme was ~10 to 12 μm. Figures 6(d) and 6(g) show a depth color-coded projection view. The pseudocolor (RGB) map codes the linearly scaled axial location of the vessels.

The superficial capillary network is observed mostly within the nerve fiber layer or the ganglion cell layer. In addition, the depth-resolved intermediate capillary plexus, between the inner plexiform layer and the inner nuclear layer as well as the deeper
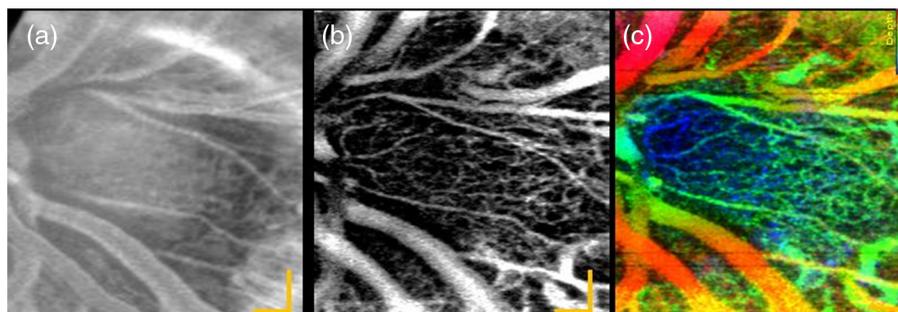

Fig. 9 Retinal capillary network at optic nerve head area (1.5 $\times$ 1.5 mm^2). (a) FA. (b) Total projection view of pvOCT (c) RGB depth color-coded projection view of pvOCT data. Upper right shows depth scale bar with red color denoting a superficial layer, green showing capillaries in an intermediate vascular bed, and finally blue represents microcapillaries as a deeper vascular layer. Scale bar: 250 μm. Video 2 shows C-scan fly through the data and Video 3 shows volumetric visualization of pvOCT data set (MOV 9058KB) [URL: http://dx.doi.org/10.1117/1.JBO.19.12.126010.2].; (MOV 2182KB) [URL: http://dx.doi.org/10.1117/1.JBO.19.12.126010.3].
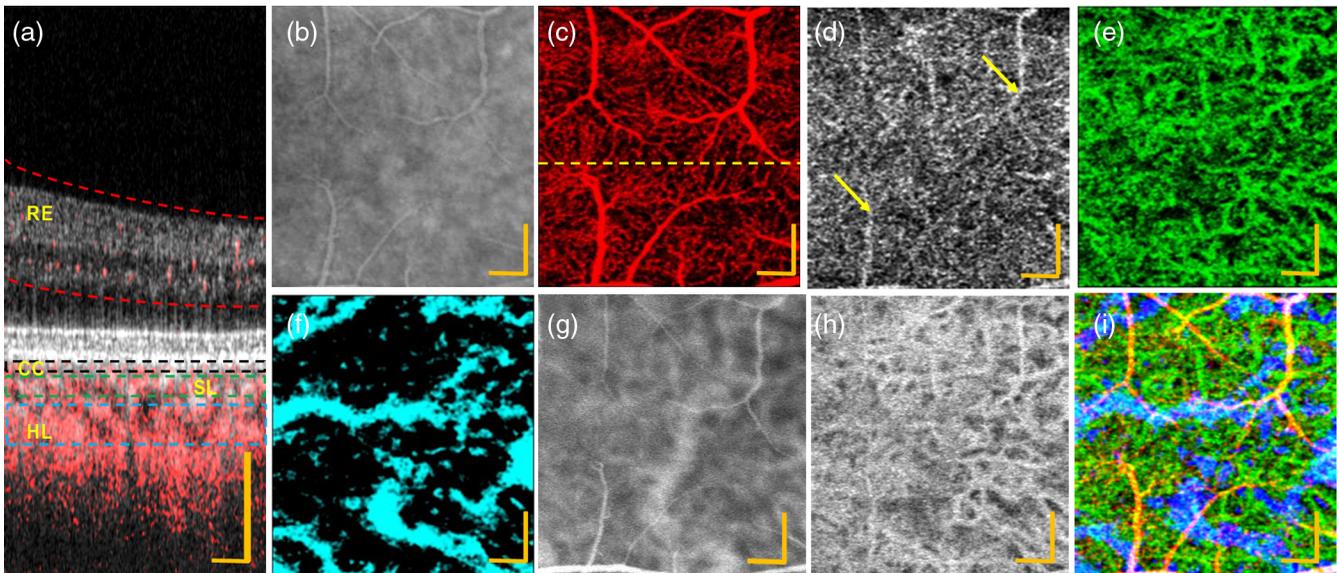
Fig. 10 pv-SSOCT volumetric scan over 1.5×1.5 mm^2 at 6-deg temporal retina (from subject 1). (a) Composite B-scan image showing flow signal in different retinal and choroidal layers overlaid over intensity image, and (b) corresponding FA image, segmented depths for *en face* projection images are: (c) retinal layers, (d) 6 μm below Bruch's membrane for choriocapillaris (e) 26 to 34 μm below Bruch's membrane for Sattler's layer; (f) 61 to 90 μm below Bruch's membrane for Haller's layer; (g) corresponding indocyanine green angiography (ICGA) image, (h) total *en face* projection of choriodal layer only in gray scale, and, (i) depth color-coded *en face* projection. Yellow arrows in (d) show the shadow artifact from large retinal vessels projected onto the choriocapillaris layer. Scale bars, 300 μm. Morphological features here resemble histological images by corrosion vascular casts and scanning electron microscopy.[27]

vascular plexus located between the outer plexiform layer and the outer nuclear layer, can be distinctly observed. The attached gray-scaled video (Video 1) demonstrates the depth morphology of the vasculature using the pvOCT data from the nerve fiber layer to the deeper choroidal layer.

A large FOV of the retinal layer was also presented to compare the corresponding FA image in Fig. 7. To maintain high-resolution in a single volume acquired in a few seconds, the scanning patterns were set to cover the 1.5×1.5-mm^2 scanning area. Several volumes were acquired at different retinal locations. Figure 7
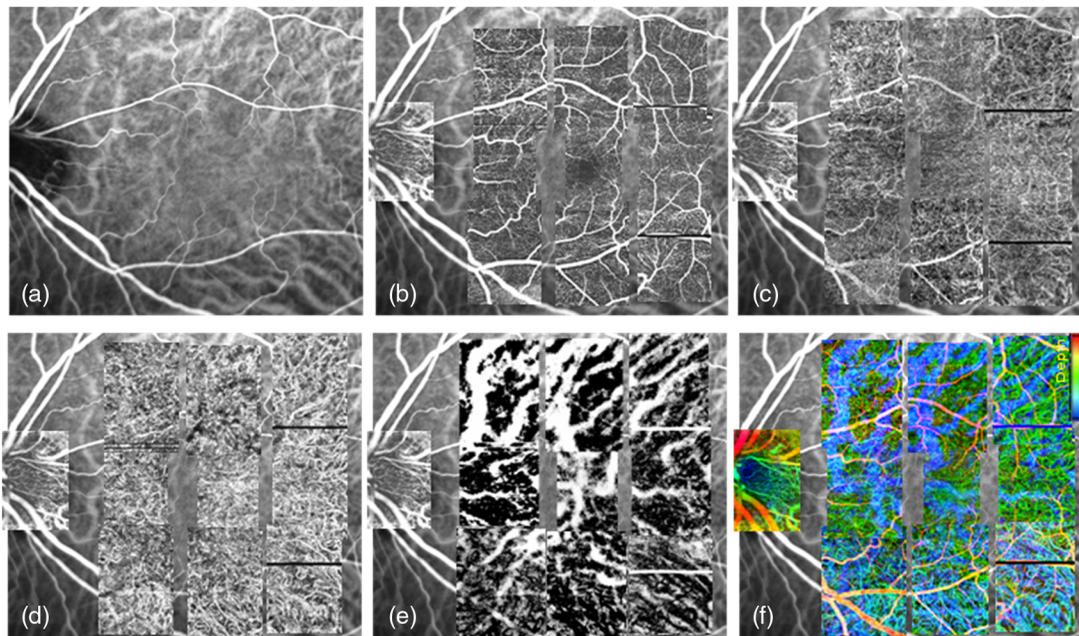

Fig. 11 Large FOV images of stitched pvSSOCT scans overlaid on a fundus ICGA (subject 1). (a) ICG angiography. (b) Projection view of retinal layers from 10 volumes, (c) stitched OCT angiograms of the choriocapillaris, (d) Sattler's layer, (e) Haller's layer, and (f) depth color-coded imaging. Upper right shows depth scale bar with red color denoting retinal vasculature, green showing Sattler's layer, and blue denoting Haller's layer.
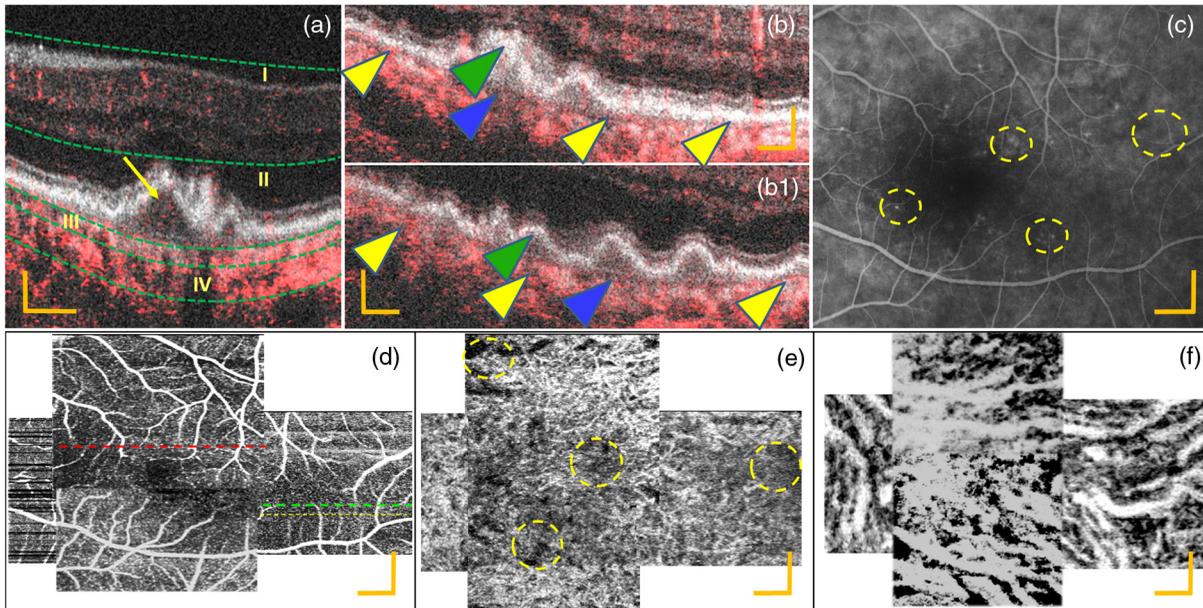
Fig. 12 pv-SSOCT imaging of P1. (a) OCT composite B-scan image at volume scan over 1.5×1.5 mm^2 at 3-deg nasal retina of the patient with age-related macular degeneration (AMD) with deformation of retinal pigment epithelium (RPE) (c, yellow dotted circle), with a retinal scan location as identified on the horizontal yellow dashed line (d). Dotted curved green line represents manual segmentation position (I-retinal layer, II-degeneration region, III-Sattler's layer and IV-Haller's layer). Yellow arrow shows deformed RPE; (b and b1) Two OCT zoomed composite B-scan images from the location of the red and green dotted lines from image (d), respectively. As indicated by the blue arrow, pv signals by micro-circulation disappeared underneath Bruch's membrane due to AMD, whereas motion contrast signals by blood perfusion (remaining choriocapillaris) exist in the region pointed by the yellow arrowhead. Green arrow head shows position of deformed RPE; (c) FA image at central foveal region; (d) projection view of retinal layers; (E) stitched OCT angiograms of Sattler's layer, yellow dotted circle represents ischemic flow region; (f) Haller's layer. (Scale bars, 300 μm and for b and b1 100 μm).

presents the large FOV image overlaid on the fundus FA. This image was made from ten 1.5×1.5 mm^2 pvOCT volumes acquired by shifting the position of light emitting diode fixation points. After pvOCT processing, each projection image was manually aligned with linear translation to create a large FOV mosaic.

Several groups have previously demonstrated images of choricapillaris and Sattler's layer with different OCT flow contrasting methods.[22,24–26] Our results are comparable to those reports. As an example, Fig. 8 shows images of the chorio-retinal perfusion of another normal eye from a different subject. A high sampling density angiogram of retinal, choriocapillaris, and Sattler's layer were shown in Figs. 8(a), 8(b), and 8(c), respectively. Figures 8(f) and 8(g) show a dense vascular network right below the fovea. Choriocapillaris is usually described as a monolayer vascular network [Figs. 8(d) and 8(e)] with a mesh-like structure with pore size ranges from 5 to 40 μm (images adapted from Olver et al.[27]). Choriocapillaris angiograms generated by our pv-SSOCT method [Figs. 8(f) and 8(g)] show a similar mesh-like network with small black pores where the pv-SSOCT signal is absent. Several pores were indicated by yellow arrows. The average cross-sectional diameters of the pores are 26 μm. This value is similar to our pore size. The pores beyond 17 μm are not visible due to limitations of the lateral resolution of our current system. From the above results and similarities between the pv-SSOCT angiogram of the choriocapillaris and the scanning electron microscopy image, we can conclude that Fig. 8(f) represents choriocapillaris perfusion.

3.3 Pv-SSOCT Vascular Network Imaging of Optic Nerve Head (ONH) Area

In vivo imaging of vasculature around the optic nerve head region was also tested with our pv-SSOCT system. A depth-resolved pv-SSOCT and corresponding FA images are compared in Fig. 9. Video 2 demonstrates depth-resolved *en face* OCT angiography and virtual C-scan fly through. Several blood vessels are visualized with the progression of scans through the optic nerve head. pv shadows created by blood vessels are clearly seen in the movie, tracking with the vessels entering the optic nerve head. The retinal capillary network (within the nerve fiber layer to the outer nuclear layer) is coded as red. The 3-D vascular network can be visualized further by generating a 3-D reconstruction of the optic nerve head (Video 3). A better visualization of branches of the vascular tree is observed compared to FA.

3.4 Comparison between ICGA and pv-SSOCT Vascular Network Imaging of Chorioretinal Complex

A comparison between pv-SSOCT projections and corresponding ICGA images is presented in Fig. 10. The flow signal from different retinal and choroidal layers has been superposed on the intensity image shown in a composite B-scan image [Fig. 10(a)]. A volumetric manual segmentation [Fig. 9(a)] was performed to extract each vascular layer based on the existing literature.[12,13,22,24] The retinal vascular network (within the nerve
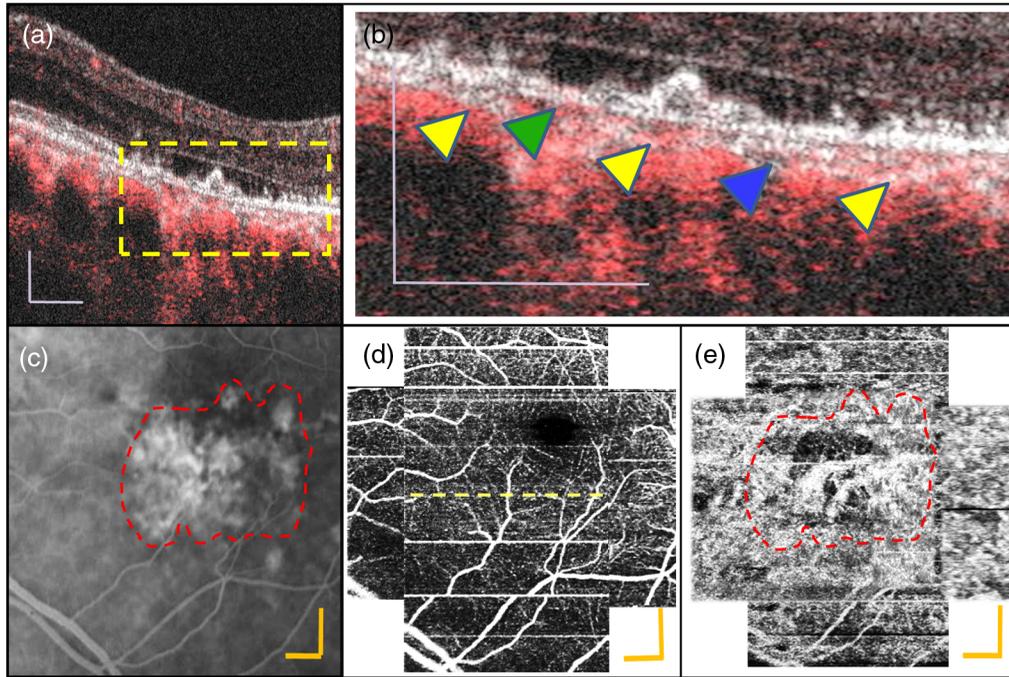
Fig. 13 pv-SSOCT imaging of P2. (a) OCT composite B-scan image at volume scan over 1.5×1.5 mm^2 at 3-deg temporal retina of the patient having reticular pseudodrusen (c, red dotted circle), with a retinal scan location as identified on the horizontal yellow dashed line (d). (b) an OCT zoomed composite B-scan images from the location of yellow dotted rectangle from image (a). As indicated by the blue arrow, pv signals by microcirculation disappeared underneath Bruch's membrane due to choriocapillaris atrophy, whereas motion contrast signals by blood perfusion (remaining choriocapillaris) exist in the region pointed by the yellow arrowhead. Green arrow head shows position of RPE; (c) FA image at central foveal region; (d) projection view of retinal layers; (e) stitched OCT angiograms of Sattler's layer, yellow dotted circle represents ischemic flow region; (Scale bars, 300 μm for a, b; for c, d, e 400 μm).
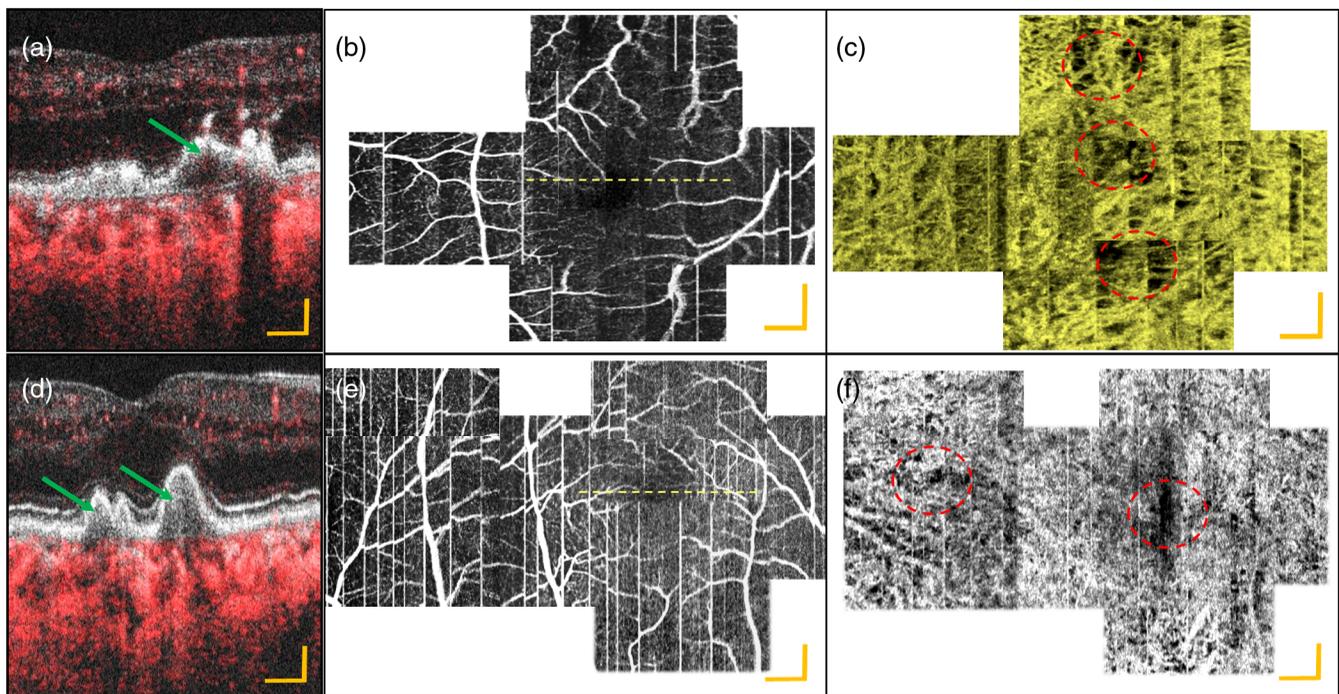

Fig. 14 pv-SSOCT imaging of P3 (upper panel) and P4 (lower panel). (a and d) OCT composite B-scan image at volume scan over 1.5×1.5 mm^2 center foveal retina of the patient having AMD, with a retinal scan location as identified on the horizontal yellow dashed line (b) and (e), respectively; green arrow shows position of atrophy and RPE deformation; (b and e) Projection view of retinal layers; (c and f) Stitched OCT angiograms of Sattler's layer, red dotted circle represents ischemic flow region; scale bars, 400 μm.

fiber layer to the outer nuclear layer) is coded as red [Fig. 10(c)]. Choriocapillaris marked at different depths (6 μm below Bruch's membrane coded as gray) were generated from the OCT pv volume [Fig. 10(d)]. Here, shadow artifacts from large retinal vessels (marked with yellow arrows) are observed. They are not a part of the choroidal vasculature. Figure 10(e) shows an *en face* angiogram extracted from the same volumetric data sets from 26 to 34 μm below Bruch's membrane, where feeding arterioles and draining venules in Sattler's layer are clearly visualized. Haller's layer, consisting of larger feeder vessels located from 61 to 90 μm below Bruch's membrane, is shown in Fig. 10(f).

To generate an *en face* map of Haller's layer, the following method was used. The segmented C-scans from Haller's layer were projected with minimum intensity, and then the image intensity scale was inverted. The reason for this image processing step was explained in Sec. 3.1. Large vessels in Haller's layer appear black (no detected flow signal) in our pv-SSOCT data. A minimum threshold was applied in the above process; hence, the displayed pvOCT signal is generated by large vessels in Haller's layer. For comparison, the ICGA [Fig. 10(g)] and corresponding pv-SSOCT total choroidal projection in gray scale [Fig. 10(h)] are presented. The pseudocolor (RGB) depth-coded projection is also presented in Fig. 10(i). There is excellent correspondence of structural features between the OCT angiograms and the electron micrograph corrosion casts reported by Olver et al.[27] Deep penetration pv-SSOCT clearly permits *in vivo* visualization of the chorioretinal complex.

To illustrate clinically applicable images of choroidal flow, a large FOV pvOCT from different choroidal layer *en face* projections overlaid on the fundus ICGA image are presented in Fig. 11.

At different retinal eccentricities, variations in choriocapillaris density and pattern are observed. A tightly packed choriocapillaris with a mesh-like structure is visualized at the central fovea [Fig. 11(c)]. However, the density is reduced at a higher eccentricity [Fig. 11(c)]. Similar kinds of variations in vessel diameter and pattern are also observed in Sattler's layer [Fig. 11(d)] as well as Haller's layer [Fig. 11(e)]. The density of the feeding vessel diameters in Sattler's layer increases as we move out from the central foveal region. Larger choroidal vessels below the choriocapillaris layer are visible in pvSSOCT *en face* images because of the deeper penetration, high sensitivity, and high phase stabilization in our SSOCT system.

A major advantage of the high penetration 1-μm pv-SSOCT technique over fluorescein or ICG angiography, similar to other OCT-based flow contrasting methods, is that it does not require any exogenous contrast agents that are uncomfortable or have occasional adverse reactions. Thus, our method is noncontact and noninvasive. Additionally, depth-resolved fine vascular structure located below the RPE can be clearly seen. The depth color-coded visualization of the retinal and choroidal vasculature shown in Fig. 11(f).which summarizes vascular maps segmented from retinal and chroidal layers: below the inner limiting membrane to the outer limiting membrane (retinal layer)—red, Sattler's layer—green, and Haller's layer—blue. Vessels present in the intermediate layer have a yellowish color.

3.5 *pv-SSOCT Vascular Network Imaging of Chorioretinal Complex in Diseased Eyes*

Four AMD patients were imaged with high penetration 1-μm pv-SSOCT. Figure 12 shows the pv-SSOCT imaging from patient 1 (AMD). The position of atrophy can be seen from Fig. 12(c) yellow dotted circle. A close look of composite flow images [Figs. 12(a), 12(b), and 12(b1)], provides detailed information under the RPE. In Figs. 12(b) and 12(b1), inconsistent choriodal flow was observed due to AMD and atrophy, and flow signals by microcirculation disappeared underneath Bruch's membrane due to AMD (blue arrows [Figs. 12(b) and 12(b1)]), whereas motion contrast signals by blood perfusion in the remaining choriocapillaris exists in the region pointed out by the yellow arrowhead. The green arrow head shows the position of the deformed RPE. Manual segmentation positions were presented as a dotted curved green line in Fig. 12(a). It was also observed that there is an absence of flow signals in the degenerative region (green arrows). The FA image [Fig. 12(c)] and corresponding mosaic view of the retinal projection layers in Fig. 12(d) are similar. Yellow circles on the angiograms of Sattler's layer [Fig. 12(e)] represent the positions of ischemic flow regions. Haller's layer was shown in Fig. 12(f).

Another patient with reticular pseudodrusen (deposits above RPE) was imaged. The position of the drusen and corresponding flows were presented in Fig. 13(a). A cropped view (yellow rectangle in [Fig 13(a)] provides detailed information about the flow within and beneath the drusen area. It was observed that the microcirculation disappeared underneath Bruch's membrane due to choriocapillaris atrophy [blue arrow [Fig. 13(b)]], but blood perfusion in the remaining choriocapillaris exist in the region pointed out by the yellow arrowhead. The green arrow head shows the position of the RPE. A well-defined capillary network in the retina [Fig. 13(d)] was observed. However, a focal disruption/loss of choriocapillaris within the area of underneath drusen and atrophy region the inner choroidal layer [Fig. 13(e)] was clearly visible for the same subject. The region was highlighted with red dotted lines and compared with the corresponding FA image [Fig. 13(c)]. However, there is no flow signal observed within the drusen area.

Alterations in chrorioretinal perfusion were also observed in layers from two other AMD patients (Fig. 14, upper panel and lower panel). There was deformation of the RPE layer for both patients [green arrow, Figs. 14(a) and 14(d)]. A well-defined flow in the retinal layer was present, as observed in Figs. 14(b) and 14(e). However, there is a loss of flow signals observed in Sattler's layer [Figs. 14(c) and 14(f)]. Missing and abnormal vessel perfusion areas were highlighted with red dashed circles in Figs. 14(c) and 14(f).

4 Conclusion

In this paper, we demonstrate the feasibility of a pv-based high-speed 1-μm SSOCT system for *in vivo*, noncontact, and noninvasive depth-resolved 2-D visualization of the vasculature of the chorioretinal complex. The pv-SSOCT produces detailed insight into vascular capillary networks comparable to fundus FA without the need for exogenous contrast agents. A densely sampled small FOV, 1.5×1.5 mm^2, allows generation of microcapillary perfusion maps with depth color-coding. The pv-SSOCT angiography is capable of generating integrated imaging of both retinal and choroidal structures and vasculature. Our data, including images acquired from normal and patient participants, suggest that pv-SSOCT has the potential to improve the early diagnosis of retinal vascular diseases including AMD and allow better understanding of disease pathogenesis as well as more detailed studies of treatment response and the efficiency of pharmaceutical agents.

References

1. Y. Imamura et al., "Enhanced depth imaging optical coherence tomography of the choroid in central serous chorioretinopathy," *Retina* **29**, 1469–1473 (2009).
2. A. Chopdar et al., "Age related macular degeneration," *Br. Med. J.* **340** (2010).
3. A. Unterhuber et al., "In vivo retinal optical coherence tomography at 1040 nm enhanced penetration into the choroid," *Opt. Express* **13**, 3252–3258 (2005).
4. R. K. Wang et al., "Multifunctional imaging of human retina and choroid with 1050-nm spectral domain optical coherence tomography at 92-kHz line scan rate," *J. Biomed. Opt.* **16**, 050503 (2011).
5. S. H. Yun et al., "Motion artifacts in optical coherence tomography with frequency-domain ranging," *Opt. Express* **12**, 2977–2998 (2004).
6. V. J. Srinivasan et al., "Ultrahigh-speed optical coherence tomography for three-dimensional and en face imaging of the retina and optic nerve head," *Invest. Ophthalmol. Vis. Sci.* **49**, 5103–5110 (2008).
7. B. Potsaid et al., "Ultrahigh speed 1050 nm swept source/Fourier domain OCT retinal and anterior segment imaging at 100,000 to 400,000 axial scans per second," *Opt. Express* **18**, 20029–20048 (2010).
8. T. Klein et al., "Megahertz OCT for ultrawide-field retinal imaging with a 1050 nm Fourier domain mode-locked laser," *Opt. Express* **19**, 3044–3062 (2011).
9. Topcon, "DRI OCT-1, Atlantis swept source OCT," http://www.topcon-medical.eu/eu/products/177-dri-oct-1-swept-source-oct.html (10 April 2013).
10. B. Baumann et al., "Total retinal blood flow measurement with ultrahigh speed swept source/Fourier domain OCT," *Biomed. Opt. Express* **2**, 1539–1552 (2011).
11. B. Braaf et al., "Phase-stabilized optical frequency domain imaging at 1-μm for the measurement of blood flow in the human choroid," *Opt. Express* **19**, 20886–20903 (2011).
12. Y. Hong et al., "High-penetration swept source Doppler optical coherence angiography by fully numerical phase stabilization," *Biomed. Opt. Express* **20**(3), 2740–2760 (2012).
13. H. C. Hendargo et al., "Doppler velocity detection limitations in spectrometer-based versus swept-source optical coherence tomography," *Biomed. Opt. Express* **2**(8), 2175–2188 (2011).
14. Y. Zhao et al., "Doppler standard deviation imaging for clinical monitoring of in vivo human skin blood flow," *Opt. Lett.* **25**, 1358–1360 (2000).
15. S. Makita et al., "Optical coherence angiography," *Opt. Express* **14**, 7821–7840 (2006).
16. Y. Yasuno et al., "In vivo high-contrast imaging of deep posterior eye by 1-um swept source optical coherence tomography and scattering optical coherence angiography," *Opt. Express* **15**, 6121–6139 (2007).
17. J. Fingler et al., "Mobility and transverse flow visualization using phase variance contrast with spectral domain optical coherence tomography," *Opt. Express* **15**, 12636–12653 (2007).
18. J. Fingler et al., "Volumetric microvascular imaging of human retina using optical coherence tomography with a novel motion contrast technique," *Opt. Express* **17**(24), 22190–22200 (2009).
19. D. Y. Kim et al., "In vivo volumetric imaging of human retinal circulation with phase-variance optical coherence tomography," *Biomed. Opt. Express* **2**, 1504–1513 (2011).
20. M. Szkulmowski et al., "Flow velocity estimation using joint spectral and time domain optical coherence tomography," *Opt. Express* **16**, 6008–6025 (2008).
21. W. J. Choi et al., "Phase-sensitive swept-source optical coherence tomography imaging of the human retina with a vertical cavity surface-emitting laser light source," *Opt. Lett.* **38**(3), 338–340 (2013).
22. W. J. Choi et al., "Choriocapillaris and choroidal microvasculature imaging with OCT angiography," *PLoS One* **8**(12), 81499–81503 (2013).
23. R. Poddar et al., "Three-dimensional anterior segment imaging in patients with type 1 Boston Keratoprosthesis with switchable full depth range swept source optical coherence tomography," *J. Biomed. Opt.* **18**(8), 086002 (2013).
24. K. Kurokawa et al., "Three-dimensional retinal and choroidal capillary imaging angiography with adaptive optics," *Opt. Express* **20**, 22796–22812 (2012).
25. Braaf et al., "Real-time eye motion correction in phase-resolved OCT angiography with tracking SLO," *Biomed. Opt. Express* **4**(1), 51–65 (2013).
26. D. Y. Kim et al., "Optical imaging of the chorioretinal vasculature in the living human eye," *Proc. Natl. Acad. Sci. U.S.A.* **110**, 14354–14359 (2013).
27. J. M. Olver et al., "Functional anatomy of the choroidal circulation: Methyl methacrylate casting of human choroid," *Eye* **4**, 262–272 (1990).

Raju Poddar is an assistant professor at the Birla Institute of Technology, Ranchi, India. He received his PhD degree in optics from the Birla Institute of Technology, India in 2009. He is author of more than 24 journal papers. His current research interests include swept-source optical coherence tomography, computational biology, and optoelectronic systems.

Daeyu Kim is an assistant professor in the Beckman Laser Institute Korea and Biomedical Engineering at the Dankook University, Korea. He received the PhD degree in biomedical engineering from the University of California, Davis, where he was a Med-into-Grad Initiative Scholar from the Howard Hughes Medical Institute. He was a postdoctoral scholar in the Biological Imaging Center, Beckman Institute, at Caltech and in the Translational Imaging Center at the University of Southern California.

John S. Werner received his PhD in experimental psychology from Brown University and conducted postdoctoral research at the Institute for Perception—TNO in Soesterberg, The Netherlands. He is currently a distinguished professor in the Department of Ophthalmology & Vision Science and Department of Neurobiology, Physiology & Behavior at the University of California, Davis. He is the author of more than 250 peer-reviewed papers and a number of books including recently published *The New Visual Neurosciences*.

Robert J. Zawadzki received BS and MS degrees in experimental physics and medical physics from the Nicolaus Copernicus University Torun, Poland, and a PhD degree in natural sciences from Technical University of Vienna, Austria. In 2004, he joined the UC Davis Vision Science and Advanced Retinal Imaging (VSRI) Laboratory, where he is now an associate researcher. He is the author of more than 60 peer-reviewed articles and 50 conference proceedings.